

# Bayesian Shear Wave Speed Reconstruction with an On-Axis ARFI Prior

Derek Y. Chan, Ned C. Rouze, Mark L. Palmeri, and Kathryn R. Nightingale  
Department of Biomedical Engineering, Duke University, Durham, NC, USA  
Email: derek.chan@duke.edu

**Abstract**—Shear wave elasticity image quality can be degraded by poor signal-to-noise ratio or spatial resolution due to low shear wave amplitudes and reconstruction kernel size. A framework is presented for incorporating additional information about relative stiffness, based on the on-axis ARFI displacement data, for enhanced shear wave speed reconstruction. Using Bayes' theorem, a prior distribution describing the expected shear wave speed based on local displacement magnitudes is combined with a likelihood function, which describes the estimated speed based on the tracked shear wave data. In a phantom, the Bayesian estimator increased range of reconstructed depths by 55% compared to a conventional cross-correlation SWEI method, and decreased SWS bias compared to the ARFI-only reconstruction. The Bayesian estimator also improved visualization of *in vivo* prostate anatomy and prostate cancer.

## I. INTRODUCTION

Tissue stiffness, which is often correlated with disease state, can be noninvasively characterized with ultrasound [1]. In shear wave elasticity imaging (SWEI), the propagation speed of shear waves created with a radiation force excitation is quantitatively related to the shear modulus [2]. The accuracy of shear wave speed reconstruction is limited in regions where the shear wave amplitudes are low, such as a very stiff material or outside the depth of field of the push excitation [3]. Furthermore, with time-of-flight estimation methods, the shear wave speed is computed over a region that is assumed to be homogeneous. The size of the reconstruction kernel can introduce artifacts or limit the spatial resolution of the resulting image [4].

On the other hand, acoustic radiation force impulse (ARFI) imaging tracks the on-axis displacement magnitudes within the region of excitation, and a 2-D displacement map is created by laterally translating the push excitations across the aperture. While ARFI only provides a measure of relative stiffness, it typically has higher resolution than SWEI, since it does not require a time-of-flight reconstruction kernel [5]. Additionally, ARFI often has improved penetration compared to SWEI, resulting from higher signal amplitudes within the region of excitation.

A previous study examined the use of a Bayesian model for reducing noise in SWEI images by using a prior distribution that enforced a spatial continuity constraint [6]. This work demonstrated reductions in the bias and variance of shear wave speed estimates compared to a conventional linear regression-based estimator. However, since the only additional information contained in the prior were the adjacent shear wave speed

estimates, this model was not designed to preserve spatial resolution or increase penetration depth in the reconstructed SWEI image.

In this work, a Bayesian framework is presented for enhancing the quality of shear wave elasticity images using a prior based on the on-axis ARFI displacement. The method is evaluated in phantom and *in vivo* prostate data obtained with a combined ARFI/SWEI sequence, and the results are compared to a conventional cross-correlation SWEI estimator.

## II. METHODS

### A. Theory

Bayes' theorem can be expressed as

$$P(c_s | x) \propto P(x | c_s) \cdot P(c_s), \quad (1)$$

where  $P(c_s | x)$  is the posterior probability density function (PDF) of the shear wave speed  $c_s$  given the observed shear wave velocity data  $x$ . The prior PDF  $P(c_s)$  incorporates prior knowledge about the shear wave speed. In this model,  $P(c_s)$  is constructed from estimates of the on-axis displacements and shear wave speeds from the local neighborhood around a given pixel.  $P(x | c_s)$  is the likelihood function which gives the probability of observing the shear wave data, assuming a certain shear wave speed  $c_s$ .

The objective is to determine the value of  $c_s$  that maximizes the posterior PDF. Since the logarithm is a strictly increasing function, it is often more computationally efficient to rewrite (1) in the log domain:

$$\ln(P(c_s | x)) \propto \ln(P(x | c_s)) + \ln(P(c_s)). \quad (2)$$

To formulate the prior PDF, the material within a given local reconstruction kernel is assumed to be linear, elastic, homogeneous, and isotropic. Given these assumptions, the shear wave speed  $c_s$  can be mathematically related to the Young's modulus  $E$ , along with the density  $\rho$  and the Poisson's ratio  $\nu$ :

$$\rho c_s^2 = \frac{E}{2(1 + \nu)}. \quad (3)$$

With further assumptions of incompressibility ( $\nu = 0.5$ ) and a density of  $1 \text{ g/cm}^3$ , this equation simplifies to  $E = 3c_s^2$ .

The on-axis displacement  $u$  is assumed to be inversely proportional to the stiffness after appropriate depth-dependent gain is applied to account for spatial gradients in the applied radiation force due to focusing and attenuation [5]. This

inverse relation between displacement and elastic modulus and the quadratic relation between shear wave speed and modulus leads to the following equation relating shear wave speed and displacement:

$$c_s = \frac{K}{\sqrt{u}} \quad (4)$$

where  $K$  is a constant that is theoretically valid for all pairs of shear wave speed and displacement values in the image. In practice, to reduce the influence of noisy pixels in the image,  $K$  is estimated from the median shear wave speed estimate and median ARFI displacement after discarding pairs for which the correlation coefficient is less than 0.80.

With these relations, the log-prior for a given pixel was formulated as

$$\ln(P(c_{s_0})) = - \left[ w_0 \left( c_{s_0} - \frac{K}{\sqrt{u_0}} \right)^2 + \sum_{j \in B} w_j \left( c_{s_0} - c_{s_j} \sqrt{\frac{u_j}{u_0}} \right)^2 \right]. \quad (5)$$

In this equation,  $c_{s_0}$  is the shear wave speed estimate at the location of interest, while  $c_{s_j}$  denotes shear wave speed estimates at locations in a local neighborhood  $B$ . Similar notation is used for the displacement at the pixel  $u_0$  and local displacements  $u_j$ .  $K$  is the estimated conversion factor between shear wave speed and displacement, and  $w_0$  and  $w_j$  are normalized weights on the local estimates based on the correlation coefficient, used to scale the relative contributions of each term based on confidence in the estimates.

For a given location, the log-likelihood function is constructed from the cross-correlation of particle velocity signals in two dimensions after 3-D directional filtering to remove reflected wave artifacts [7], [8]. For a more robust estimate of arrival time, data from multiple push excitations were combined with a weighted algorithm based on the correlation coefficients [9].

By using this formulation, a separate probability distribution of the shear wave speed for each pixel in the image is obtained. For example, Figure 1 shows likelihood probability distributions for a series of lateral positions for data obtained in an elasticity phantom. The phantom contained a stiff inclusion around 6.4 mm laterally, demonstrated by the higher shear wave speeds in the figure. Taking the speed with maximum probability at each location (solid black line in Fig. 1) results in the maximum likelihood estimate of the shear wave speed.

### B. Phantom Data

The data used in this analysis were acquired using a Siemens SC2000 scanner (Siemens Healthcare, Mountain View, CA) with an Acuson ER7B linear side-fire probe. The radiation force excitation used three focal depths at 30 mm, 22.5 mm, and 15 mm [10]. In-phase and quadrature ( $I/Q$ ) were obtained using 16:1 parallel receive, with the four center beams used to track the on-axis displacement [11]. Six beams on either side of the excitation were used to track the shear waves, with

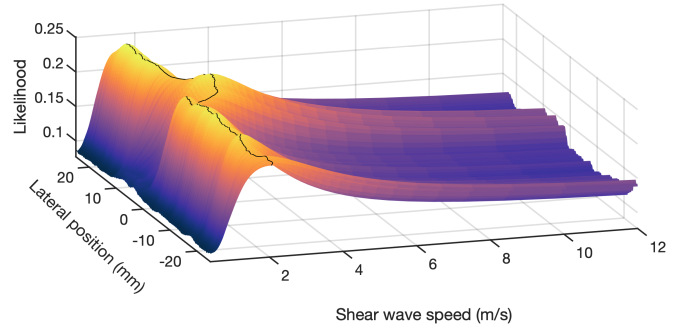


Fig. 1: Example likelihood probability distributions versus lateral position in a phantom with a 10-mm diameter stiff inclusion around 6.4 mm laterally. The higher shear wave speed distributions can be observed in the region of the inclusion.

0.76 mm between adjacent beams. Eighty-two push excitations were transmitted across the lateral field of view.

The phantom imaging target was a custom CIRS elastic phantom (Norfolk, VA) that contained a stiff cylindrical inclusion with a diameter of 10 mm and a Young's modulus of 18 kPa, corresponding to a quoted shear wave speed of 2.45 m/s according to (3). The background had a Young's modulus of 8 kPa (quoted speed of 1.63 m/s).

The *in vivo* human prostate data were obtained using the same combined ARFI/SWEI sequence described above, in an institutional review board-approved study [12]. Three-dimensional prostate ARFI/SWEI volumes were obtained in men expecting radical prostatectomy by mechanically rotating the transducer in 1 degree elevational increments using a rotation stage.

For the ARFI data, displacements were estimated using Loupas's algorithm with a 4-wavelength kernel and progressive referencing [13], [14]. Data from the third time step after the push were used, and depth-dependent gain was applied using a normalization curve from a homogeneous phantom.

For the SWEI data, velocity profiles through time were estimated with Loupas's algorithm applied to consecutive time steps, again with a 4-wavelength kernel. The data were filtered with a 2nd-order zero-phase Butterworth filter (1.5 kHz cutoff frequency), and upsampled by a factor of 5 using spline interpolation.

Contrast-to-noise ratio ( $CNR$ ) was computed using the following equation:

$$CNR = \frac{\mu_{in} - \mu_{out}}{\sqrt{\sigma_{in}^2 + \sigma_{out}^2}}. \quad (6)$$

To quantify the range of depths that was able to be reconstructed with high fidelity, this range was defined as the depths over which the median shear wave speed, averaged laterally, remained within five percent of the quoted shear wave speed. The range was computed in a homogeneous background region of the phantom. This metric was defined due to the bias in

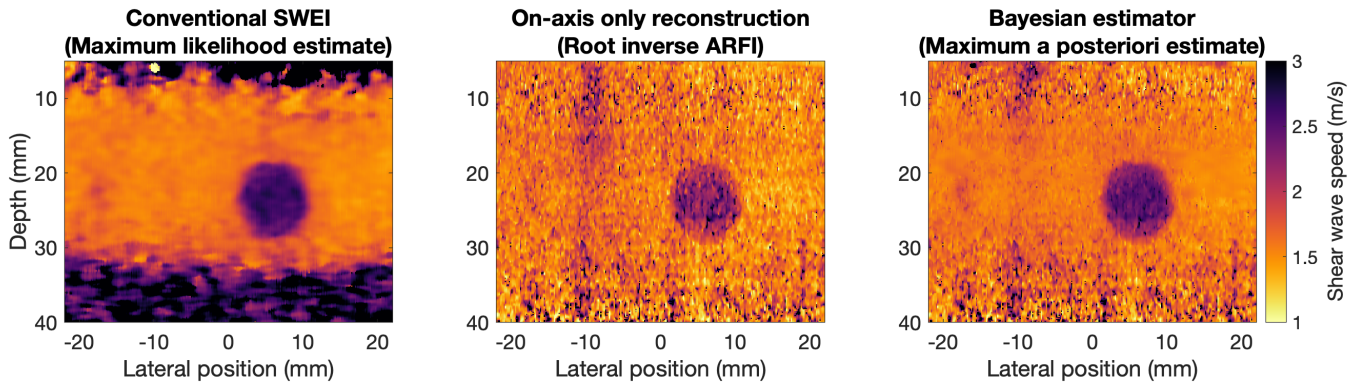


Fig. 2: (Left) Conventional cross-correlation-based SWEI reconstruction in a phantom with a stiff inclusion (maximum likelihood estimation). (Middle) Reconstruction of the SWEI image using only the on-axis displacement information, equivalent to taking the square root of the reciprocal of the ARFI displacements. (Right) Result of using the Bayesian estimator to combine the on- and off-axis information.

speeds often seen at very shallow or very deep depths, where the signal-to-noise ratio is low.

### III. RESULTS AND DISCUSSION

Figure 2 shows reconstructed images of the phantom containing a stiff inclusion. The left image displays the conventional SWEI reconstruction resulting from taking the maximum likelihood estimate of the shear wave speed at each pixel. The mean reconstructed speed in the inclusion was  $2.47 \pm 0.11$  m/s, while the mean reconstructed speed in the background was  $1.60 \pm 0.04$  m/s. The CNR of the inclusion was calculated to be 9.13.

The center image shows the on-axis-only reconstruction, equivalent to taking the square root of the inverse of the ARFI displacements. The mean reconstructed speed in the inclusion was  $2.23 \pm 0.26$  m/s, while the mean reconstructed speed in the background was  $1.69 \pm 0.16$  m/s. The CNR of the inclusion was calculated to be 1.76. Note that the large difference in CNR is due to the relative amount of noise in the middle image. However, there are inaccurate shear wave speed estimates in the SWEI image below 30 mm or above 10 mm due to poor signal-to-noise ratio. On the other hand, the root inverse ARFI image is much more consistent through depth, though there is more bias in the estimates.

The right image in Figure 2 shows the result of applying the Bayesian estimator to combine the SWEI and ARFI data, also known as the maximum *a posteriori* estimate. The mean reconstructed speed in the inclusion was  $2.42 \pm 0.15$  m/s, while the mean reconstructed speed in the background was  $1.61 \pm 0.07$  m/s. The CNR of the inclusion was 4.95; this lower CNR compared to conventional SWEI is due to increased variability in the estimates when the ARFI displacement data are incorporated. However, using this technique resulted in preservation of the extended range of depths over which shear wave speeds can be reasonably reconstructed, while maintaining accuracy in the estimated speeds.

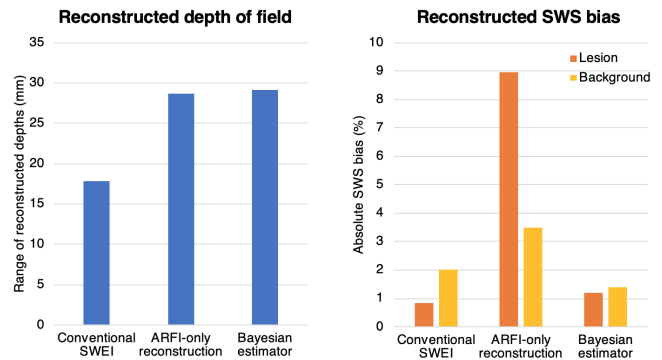


Fig. 3: (Left) Range of reconstructed depths in phantom data for conventional SWEI, ARFI-only reconstruction, and Bayesian estimator. (Right) Degrees of reconstructed SWS bias in the phantom lesion and background for conventional SWEI, ARFI-only reconstruction, and Bayesian estimator.

To further quantify these results, the left plot in Figure 3 shows the reconstructed depth of field for each approach as previously defined. With conventional SWEI, this range is low (17.8 mm) due to the poor penetration. ARFI has a much larger range (28.7 mm), and the Bayesian estimator preserves this large range (29.2 mm). The right plot shows the magnitude of the bias in shear wave speed estimates. While the ARFI estimates have a large bias (inclusion 9.0%, background 3.5%), likely due to issues in assumptions regarding the conversion factor  $K$ , both the conventional SWEI (inclusion 0.8%, background 2.0%) and proposed Bayesian estimators (inclusion 2.0%, background 1.4%) maintain a low bias.

Figure 4 shows results of the Bayesian estimator applied to one of the subjects in the prostate imaging study. The central gland of the prostate, indicated by the white arrow, has more uniform and distinct edges with the Bayesian reconstruction, along with a more symmetric shape that would be expected

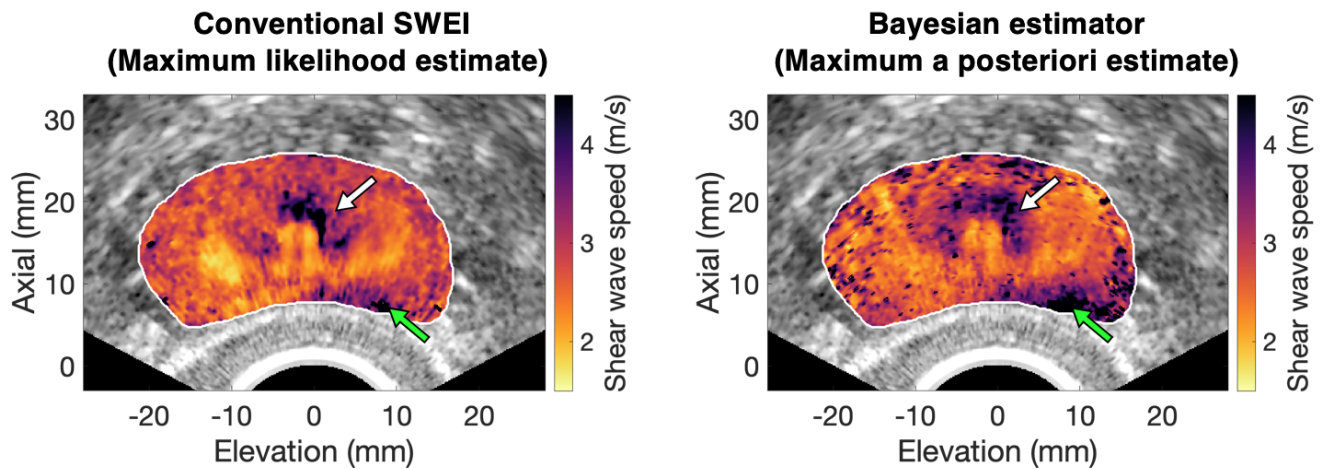


Fig. 4: (Left) *In vivo* SWEI image without incorporating ARFI data; penetration depth and contrast are limited. (Right) Combining ARFI and SWEI increased CNR in the central zone (white arrow) from 0.91 to 1.86 and increased contrast in a cancerous lesion (green arrow).

for the prostate. The anterior edge of the central zone is shown more clearly with the Bayesian estimator due to the improved depth penetration. Combining ARFI and SWEI increased CNR in the central zone from 0.91 to 1.86 and increased contrast in a histologically-confirmed prostate cancer lesion (green arrow).

The processing time for the Bayesian algorithm is currently slower than the processing time for conventional SWEI, since there are the added steps of incorporating the ARFI prior information and optimization of the cost function. While a compute cluster was used for parallel processing of the data in this study, future work will explore more efficient computation methods, such as pre-calculation of the analytic derivatives to accelerate the gradient descent optimization process.

#### IV. CONCLUSIONS

In this study, a novel method for combining on-axis ARFI displacement data with off-axis shear wave data using Bayes' theorem was presented. Under specific assumptions, both sets of data can be related via the elastic modulus of the material. This approach yields a high-quality SWEI reconstruction with improved contrast and depth penetration, compared to a conventional SWEI approach. This Bayesian estimator was applied to phantom data, where penetration depth was improved compared to conventional SWEI, and *in vivo* data to improve visualization of prostate cancer and prostate anatomy.

#### ACKNOWLEDGMENTS

This work was supported by NIH grant R01-CA142824 and DOD PCRP grant W81XWH-16-1-0653. The authors thank Siemens Medical Solutions USA, Ultrasound Division for kind and technical support.

#### REFERENCES

[1] P. N. Wells and H. D. Liang, "Medical ultrasound: imaging of soft tissue strain and elasticity," *J. R. Soc. Interface*, vol. 8, no. 64, pp. 1521–1549, Nov. 2011.

[2] A. P. Sarvazyan et al., "Shear wave elasticity imaging: a new ultrasonic technology of medical diagnostics," *Ultrasound Med. Biol.*, vol. 24, no. 9, pp. 1419–1435, Dec. 1998.

[3] Y. Deng et al., "Analyzing the impact of increasing Mechanical Index (MI) and energy deposition on shear wave speed (SWS) reconstruction in human liver," *Ultrasound Med. Biol.*, vol. 41, no. 7, pp. 1948–1957, July 2015.

[4] N. C. Rouze, M. H. Wang, M. L. Palmeri, and K. R. Nightingale, "Parameters affecting the resolution and accuracy of 2D quantitative shear wave images," *IEEE Trans. Ultrason. Ferroelectr. Freq. Control*, vol. 59, no. 8, pp. 1729–1740, Aug. 2012.

[5] K. Nightingale, "Acoustic radiation force impulse (ARFI) imaging: a review," *Curr. Med. Imaging Rev.*, vol. 7, no. 4, pp. 328–339, Nov. 2011.

[6] S. J. Rosenzweig et al., "Bayesian shear wave speed estimation for *in vivo* 3D imaging of the prostate," *Proc. IEEE Int. Ultrason. Symp.*, pp. 1260–1263, July 2013.

[7] S. L. Lipman, N. C. Rouze, M. L. Palmeri, and K. R. Nightingale, "Evaluating the improvement in shear wave speed image quality using multidimensional directional filters in the presence of reflection artifacts," *IEEE Trans. Ultrason. Ferroelectr. Freq. Control*, vol. 63, no. 8, pp. 1049–1063, Aug. 2016.

[8] P. Song et al., "Fast shear compounding using robust 2-D shear wave speed calculation and multidirectional filtering," *Ultrasound Med. Biol.*, vol. 40, no. 6, pp. 1343–1355, June 2014.

[9] D. Y. Chan et al., "Prostate shear wave elastography: multiresolution reconstruction dependence on push beam spacing," *Proc. IEEE Int. Ultrason. Symp.*, pp. 1–4, Oct. 2018.

[10] J. Bercoff, M. Tanter, and M. Fink, "Supersonic shear imaging: a new technique for soft tissue elasticity mapping," *IEEE Trans. Ultrason. Ferroelectr. Freq. Control*, vol. 51, no. 4, pp. 396–409, Apr. 2004.

[11] J. J. Dahl et al., "A parallel tracking method for acoustic radiation force impulse imaging," *IEEE Trans. Ultrason. Ferroelectr. Freq. Control*, vol. 54, no. 2, pp. 301–312, Feb. 2007.

[12] M. L. Palmeri et al., "Identifying clinically significant prostate cancers using 3-D *in vivo* acoustic radiation force impulse imaging with whole-mount histology validation," *Ultrasound Med. Biol.*, vol. 42, no. 6, pp. 1251–1262, June 2016.

[13] T. Loupas, J. T. Powers, and R. W. Gill, "An axial velocity estimator for ultrasound blood flow imaging, based on a full evaluation of the Doppler equation by means of a two-dimensional autocorrelation approach," *IEEE Trans. Ultrason. Ferroelectr. Freq. Control*, vol. 42, no. 4, pp. 672–688, July 1995.

[14] G. F. Pinton, J. J. Dahl, and G. E. Trahey, "Rapid tracking of small displacements with ultrasound," *IEEE Trans. Ultrason. Ferroelectr. Freq. Control*, vol. 53, no. 6, pp. 1103–1117, June 2006.